RSC Advances

PAPER

View Article Online
View Journal | View Issue

Check for updates

Cite this: *RSC Adv.*, 2019, **9**, 31728

TiO_2 nanocrystals with the {001} and {101} facets co-exposed with MIL-100(Fe): an egg-like composite nanomaterial for efficient visible light-driven photocatalysis†

Wan Wu, Jie Zhu, Yue Hong Deng, Ye Xiang, Ya Wen Tan, Hai Qin Tang, Hao Zou, Yi Feng Xu and Yi Zhou *

The exposure of a specific crystal face to a specific composition or a suitable carrier composition with synergistic effects can effectively improve the photocatalytic activity of the material and enhance its practical value. For choosing an ideal carrier, the primary factor is a large specific surface area. Herein, by using MIL-100(Fe) as the carrier, an egg-like TiO_2/MIL-100(Fe) composite was successfully prepared, for the first time, *via* a facile two-pot hydrothermal method. XRD, SEM, TEM and other characterization methods showed that when the molar ratio of Ti : Fe was 0.3 : 1, the morphology of the TiO_2/MIL-100(Fe) composite was completely egg-like. The TEM results showed that the {001} and {101} facets of TiO_2 in the TiO_2/MIL-100(Fe) composite were co-exposed. The BET results showed that the TiO_2/MIL-100(Fe) composite had a large specific surface area and pore size. The larger pore size provided an effective channel for the photocatalytic degradation of MB and the interfacial effect of TiO_2 and MIL-100(Fe). The separation efficiency of the photogenerated electron–hole pairs was effectively improved. The efficiency of 30% TiO_2/MIL-100(Fe) in the photocatalytic degradation of MB reached 99.02% in 30 min under visible light. All these findings showed that the composite of the effectively charge-separated photocatalytic semiconductor and the porous MOF with a high specific surface area had a high potential application value for the photocatalytic degradation of organic pollutants.

Received 14th August 2019
Accepted 16th September 2019

DOI: 10.1039/c9ra06359e

rsc.li/rsc-advances

Open Access Article. Published on 07 October 2019. Downloaded on 5/22/2026 4:35:28 AM.
This article is licensed under a Creative Commons Attribution-NonCommercial 3.0 Unported Licence.

1. Introduction

Nowadays, environmental pollution caused by organic dyes in wastewater is becoming more serious.[1–5] The design and self-assembly of novel, efficient, and highly stable photocatalysts are critical to solving the current environmental energy problems.[6–9] TiO_2 has been widely used for water decomposition and the photocatalytic degradation of organic pollutants because of its chemical stability, strong oxidizing power, non-toxicity and low-cost.[2–5,10] Large-scale commercial applications are still difficult in research at present. Moreover, the adsorption capacity of TiO_2 is poor, the specific surface area is small, and the rapid recombination of photoexcited electron–hole pairs is also a factor that causes its low photocatalytic efficiency.[11,12] Researchers have used many methods to improve and enhance the photocatalytic performance of TiO_2. For instance, precious metal loading, quantum dot doping, semiconductor recombination, and different heterojunction structures improve the photocatalytic properties of materials to some extent.[13–15] In particular, the synergistic effect of the {001} and {101} crystal facets of anatase TiO_2 and the crystal face heterojunction theory have proven that the photocatalytic properties of the facet-controlled TiO_2 material are improved.[14–17,44–46] However, high-efficiency TiO_2-based photocatalytic materials have been rarely reported thus far.

Metal-organic frameworks (MOFs) are bridged by metal ions or metal clusters with organic ligands containing O or N, forming 1D, 2D or 3D coordination porous crystal materials, which together possess the advantages of organic and inorganic compounds.[18–21] An ideal carrier is a solid matrix with a large specific surface area.[22] The advantages of MOFs as photocatalysts are their diversity, ideal ordered structure and high surface area, and they have considerable application potential in adsorption and catalysis.[20–25] Notably, several MOF species, such as MIL-101(Fe),[26–28] NH_2-UiO-66 (ref. 29–32) and NH_2-MIL-125(Ti),[33–36] and various MOF-semiconductor composites, such as TiO_2@-MIL-101,[37–39] $CsPbBr_3$ dots/UiO-66(NH_2),[40] $ZnIn_2S_4$@NH_2-MIL-125(Ti)[41] and Fe_3O_4@MIL-100(Fe),[42] are widely studied in the photocatalytic degradation of pollutants. The sandwich-like TiO_2NS@MIL-100(Fe) nanocomposite obtained by the self-assembly of TiO_2NS on porous MIL-100(Fe) not only has a porous channel to adsorb organic molecules, but the interface

Department of Chemistry and Food Engineering, Changsha University of Science and Technology, Changsha 410114, China. E-mail: zhouyihn@aliyun.com; zhouyihn@163.com

† Electronic supplementary information (ESI) available. See DOI: 10.1039/c9ra06359e

This journal is © The Royal Society of Chemistry 2019

Open Access Article. Published on 07 October 2019. Downloaded on 5/22/2026 4:35:28 AM.
This article is licensed under a Creative Commons Attribution-NonCommercial 3.0 Unported Licence.

of the composite also provides a platform for photoexcited electrons. Consequently, the photoelectron–hole separation increased, the photocatalytic performance of the material was enhanced, and the adsorption performance was also improved.[43] The MIL-100(Fe)/P25 composite photocatalyst was formed by a process in which MIL-100(Fe) was grown on the TiO_2 surface, and several Ti atoms were replaced by Fe atoms, thereby resulting in a change in the electron density distribution and defect levels.[4] In the photocatalytic process, the excited electrons were trapped at the defect level, which considerably suppressed the recombination of the charge carriers and increased the number of charge carriers, thereby improving the photocatalytic efficiency. When special TiO_2@MIL-101 core–shell nanocomposites were used as adsorbents and catalysts, the adsorption capacity was outstanding and good catalytic performance was also exhibited.[37]

Herein, an egg-like TiO_2/MIL-100(Fe) composite nanomaterial was successfully synthesized, for the first time, *via* a facile two-pot hydrothermal method, and anatase TiO_2 had the {001} and {101} facets co-exposed. The synthesised TiO_2/MIL-100(Fe) composite could efficiently photocatalyse the organic dye methylene blue (MB) under visible light ($\lambda = 664$ nm). The outstanding photocatalytic properties of the composite can be attributed to the introduction of facet-controlled TiO_2 in porous MIL-100(Fe) with a high surface area. At the same time, the increased surface area and average pore size of the TiO_2/MIL-100(Fe) composite effectively improved its photocatalytic properties, which was different from those reported in previous studies. Amongst these composites, the 30% TiO_2/MIL-100(Fe) composite exhibited the most complete egg-like morphology and had high photocatalytic performance. The efficiency of MB degradation could reach 99.02% in 30 min, and the kinetic rate was 0.158 min^{-1}, which is 2.1 and 4.3 times those of pure TiO_2 (0.036 min^{-1}) and MIL-100(Fe) (0.077 min^{-1}), respectively.

2. Experimental details

2.1 Synthesis of MIL-100(Fe)

The MIL-100(Fe) was synthesized *via* a simple hydrothermal method.[43,47] $FeCl_3 \cdot 6H_2O$ (18 mmol), H_3BTC (12 mmol) and Na_2CO_3 (25 mmol) were added into Milli-Q water (36 mL) and stirred well. Then, the mixture was poured into a 100 mL Teflon-lined steel autoclave at 160 °C for 12 h. After naturally cooling to room temperature, the light orange solid was recovered by centrifugation. In order to remove the unreacted H_3BTC, which was present both inside and outside the pores of the material, the reaction product was purified by consequent washing with hot Milli-Q water and hot ethanol several times. After centrifugation, the product was finally dried overnight at 60 °C. To prevent any experimental error, the synthesis of each material was repeated several times, and the samples were subjected to the same characterization techniques.

2.2 Synthesis of the {001} and {101} co-exposed TiO_2/MIL-100(Fe) composite

The synthesis method of the {001} and {101} co-exposed TiO_2/MIL-100(Fe) egg-like composite was similar to the above method for MIL-100(Fe). The only difference was that {001} and {101} co-exposed TiO_2 (1.8, 3.6, 5.4, and 7.2 mmol) was added to the reaction precursor during the synthesis process. The purification process was adopted from the above method.

2.3 Characterization

X-ray powder diffraction analysis (XRD) was performed on a German Bruker D8 type. The experimental conditions were Cu Kα radiation, the tube pressure and tube flow were 35 kV and 30 mA, respectively, and the scanning range was $2\theta = 5$–$70°$. Scanning Electron Microscopy (SEM) was performed using the model MAIA 3 XMH. The transmission electron microscope (TEM) model JEM-2100F with an acceleration voltage of 200 kV and produced by the Japanese Electronics Society was employed. The UV-Vis-DRS model UV-2600 produced by Shimadzu Corporation of Japan was used with $BaSO_4$ as the standard reference with a scanning wavelength range of 200–800 nm and a scan step size of 1 nm. X-ray photoelectron spectroscopy (XPS) was conducted on an EXCALAB210 produced by the American Thermoelectric Corporation. The UV-Vis spectrophotometer (model UVmini-1240) manufactured by Shimadzu Corporation of Japan was used for measuring the absorbance of methylene blue solution in the wavelength range of 200–800 nm.

2.4 Evaluation of photocatalytic activity

The photocatalytic performance of the TiO_2/MIL-100(Fe) photocatalyst was evaluated by the photodegradation of methylene blue dye (MB). 5 mg of TiO_2/MIL-100(Fe) photocatalyst was mixed with 100 mL of MB aqueous solution (10 ppm). A xenon lamp was used as the analog light source, and the dark adsorption experiment was performed for 1 h before the light was turned on, and the adsorption–desorption equilibrium was achieved between the photocatalyst and the contaminant. 3 mL of the suspension was centrifuged at 8000 rpm for 5 min, and the supernatant was taken for the measurement of absorbance at $\lambda = 664$ nm using a UV-visible spectrophotometer (UV-2550, Shimadzu).

3. Results and discussion

3.1 Structural and morphological characterization

The XRD patterns of bare TiO_2 nanoparticles, MIL-100(Fe) and TiO_2/MIL-100(Fe) with different molar ratios of components 100 (Fig. 1) depicted characteristic structures. All the peaks of pure TiO_2 at 25.28°, 37.80°, 48.05°, 53.89° and 55.06° corresponded to the (101), (004), (200), (105) and (211) crystal facets of anatase TiO_2. They depicted the characteristic tetragonal structure of anatase TiO_2 (JCPDS card no. 21-1272). The characteristic peak of MIL-100(Fe) was consistent with those in the previous reports.[43,47] After the simple hydrothermal TiO_2 modification on MIL-100(Fe), the XRD patterns of the TiO_2/MIL-100(Fe) composites with different molar ratios contained unique peaks for both TiO_2 and MIL-100(Fe) (*e.g.* $2\theta = 11.0°$, 25.2°, 37.8°, 48.0°, and 53.8°). With the increase in added TiO_2, the unique peak of TiO_2/MIL-100(Fe) at 25.28° was evident, thereby

Open Access Article. Published on 07 October 2019. Downloaded on 5/22/2026 4:35:28 AM.
This article is licensed under a Creative Commons Attribution-NonCommercial 3.0 Unported Licence.

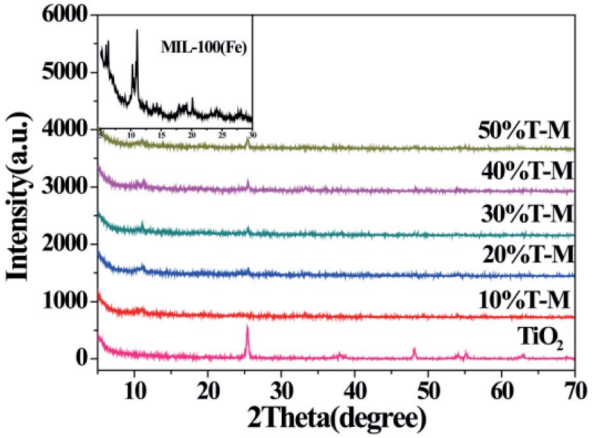

Fig. 1 XRD patterns of {001} and {101} co-exposed TiO_2 and 10–50% TiO_2/MIL-100(Fe) composites; the inset is the enlarged XRD pattern of MIL-100(Fe) in the region of $2\theta = 5–30°$.

corresponding to the {101} crystal plane of anatase TiO_2. This result demonstrated the successful modification of TiO_2 on the MIL-100(Fe) materials. The XRD pattern of the TiO_2/MIL-100(Fe) material also retained the characteristic peak of MIL-100(Fe), indicating that the composite retained the typical crystal structure of MIL-100(Fe).

The BET results indicated the porous nature of MIL-100(Fe) and the 30% TiO_2/MIL-100(Fe) composite. Fig. 2 shows the specific surface area and pore size distribution curves of the MIL-100(Fe) and 30% TiO_2/MIL-100(Fe) materials. According to the BDDT classification, both samples belonged to type II isotherm, which also indicated that all the materials prepared had porous structures. Surprisingly, with the addition of TiO_2, the specific surface area did not decrease and the pore size increased slightly, which is in agreement with the XRD results. According to previous reports, the average specific surface area of pure P25 is 53 $m^2\ g^{-1}$.[4] The average specific surface area of the 30% TiO_2/MIL-100(Fe) composite was 460.56 $m^2\ g^{-1}$. The porous 30% TiO_2/MIL-100(Fe) composite with high specific surface area and large pore size can adsorb additional organic molecules when used as a photocatalyst and accelerate the photogenerated carrier separation, thereby improving the photocatalytic performance of the material (Table 1).

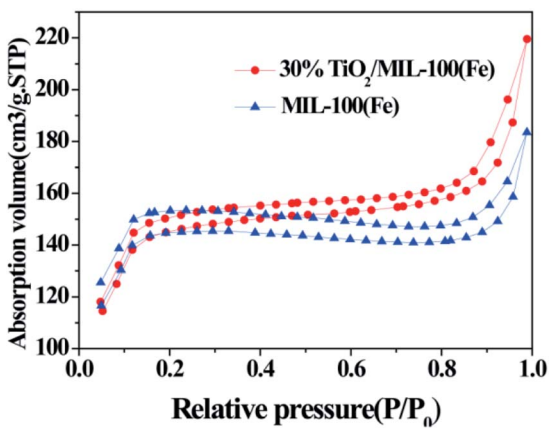

Fig. 2 N_2 adsorption–desorption isotherms of {001} and {101} co-exposed TiO_2 and the 30% TiO_2/MIL-100(Fe) composite.

The SEM and TEM images illustrated the influence of MIL-100(Fe) introduction on the morphological characteristics of the {001} and {101} co-exposed TiO_2 samples (Fig. 3, S1 and S2†). TiO_2 with co-exposed of {001} and {101} facets was successfully loaded on the surface of MIL-100(Fe), and the egg-like TiO_2/MIL-100(Fe) was established well (Fig. 3(a)–(d), S1(a), (b) and S2†). Evident lattice fringes could be observed by HRTEM (Fig. 3(d)). The lattice fringe was 0.354 nm in size, corresponding to the {101} crystal plane of TiO_2, and d = 0.235 nm corresponded to the {001} facet of TiO_2. The crystal faces demonstrated the co-exposure of the {001} and {101} facets of TiO_2 in the TiO_2/MIL-100(Fe) composites. The element distribution maps further showed that the Fe and Ti elements were uniformly distributed on the TiO_2/MIL-100(Fe) samples, thereby indicating that TiO_2 was uniformly distributed on the MIL-100(Fe) carrier, which is consistent with the SEM results. The appearance of the characteristic peaks of Fe, Ti and O on the EDS map further demonstrated the successful preparation of TiO_2/MIL-100(Fe) composites. TiO_2 was also a factor in accelerating the photogenerated electron–hole pair separation due to the synergistic effect of the crystal plane between the {001} and {101} facets, which further explains the efficient photocatalytic performance of the {001} and {101} co-exposed TiO_2/MIL-100(Fe) composites.

The chemical composition and binding status of neat TiO_2 and TiO_2@30%MIL-100(Fe) were measured by XPS. The survey spectrum (Fig. 4(a)) showed the presence of Ti, Fe, O and C. The high resolution XPS spectrum of O 1s consisted of three component peaks at 531.4 eV, 530.4 eV and 528.8 eV (Fig. S3(a)†). The characteristic binding energy peaks at 458.8 eV and 464.5 eV corresponded to Ti $2p_{3/2}$ and Ti $2p_{1/2}$ of Ti atoms, which belong to Ti^{4+} in a tetragonal structure (Fig. S3(b)†).[14] An additional peak appeared at 458.1 eV in the presence of the Fe–O–Ti bond. The Fe–O–Ti bond is formed during the growth of TiO_2/MIL-100(Fe), in which some of the Ti atoms are replaced by Fe atoms. As shown in Fig. 4(b), the peaks of Fe $2p_{3/2}$ and Fe $2p_{1/2}$ were observed at 711.9 eV and 724.8 eV, respectively, thereby indicating that the Fe element in TiO_2/MIL-100(Fe) existed in the form of Fe^{3+}.[47]

In order to further explore the factors affecting the photocatalytic activity of TiO_2/MIL-100(Fe), UV-visible absorption spectroscopy was performed for TiO_2, MIL-100(Fe) and the TiO_2/MIL-100(Fe) composites with different molar ratios. The as-prepared TiO_2 had an absorption wavelength of approximately

Table 1 BET surface area of the {001} and {101} co-exposed TiO_2 and 30% TiO_2/MIL-100(Fe) composite

Samples	BET surface area ($m^2\ g^{-1}$)	Pore volume ($cm^3\ g^{-1}$)	Pore size (nm)
MIL-100(Fe)	431.9545	0.2380	5.7786
30% TiO_2/MIL-100(Fe)	460.5602	0.2809	6.0852

This journal is © The Royal Society of Chemistry 2019

Open Access Article. Published on 07 October 2019. Downloaded on 5/22/2026 4:35:28 AM.
This article is licensed under a Creative Commons Attribution-NonCommercial 3.0 Unported Licence.

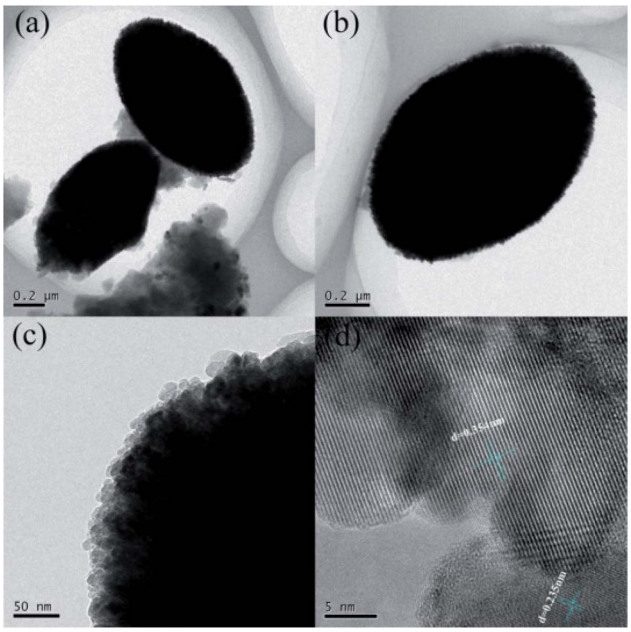

Fig. 3 TEM images of the 30% {001} and {101} co-exposed TiO_2/MIL-100(Fe) composite. (a and b) Different perspectives, (c) edge position, (d) lattice spacing.

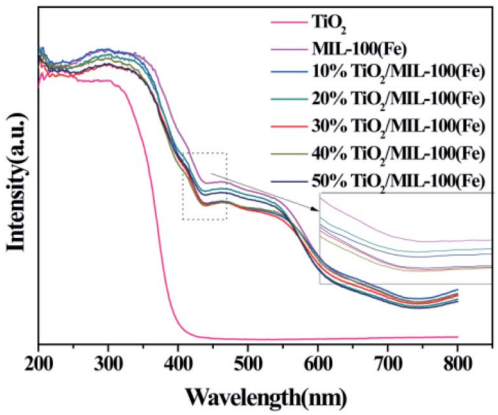

Fig. 5 UV-vis DRS spectra of TiO_2, MIL-100(Fe) and TiO_2/MIL-100(Fe) composites.

400 nm and belonged to the intrinsic absorption band (Fig. 5). In addition, MIL-100(Fe), as a carrier, also played an important role in the light absorption properties of the TiO_2/MIL-100(Fe) composites. MIL-100(Fe) and 10–50% TiO_2/MIL-100(Fe) composites had two absorption edges at 500 nm and 650 nm.

3.2 Photocatalytic activities

The photocatalytic properties of TiO_2, MIL-100(Fe) and the TiO_2/MIL-100(Fe) materials with different molar ratios of TiO_2 were investigated by the adsorption degradation of the organic dye MB under visible light. As shown in Fig. 6(a), MIL-100(Fe) and the TiO_2/MIL-100(Fe) materials with different molar ratios of TiO_2 had significant improvement compared with the photocatalyst and pure TiO_2. With the addition of TiO_2, the photocatalytic MB degradation efficiency of the TiO_2/MIL-100(Fe) composites were significantly higher than that of MIL-100(Fe). The order of degradation efficiency was as follows: 30% T/M > 40% T/M > 20% T/M > 50% T/M > 10% T/M > MIL-100(Fe) > TiO_2. The 30% TiO_2/MIL-100(Fe) composite containing {001} and {101} facet co-exposed TiO_2 exhibited the best photocatalytic performance with a degradation efficiency of 99.02% in 30 min. According to the photocatalytic experimental data, a quasi-first-order kinetic equation and the degradation rate constants for MB degradation and adsorption were obtained according to $-\ln(C/C_0) = kt$,[16,17] as shown in Fig. 6(b), (c) and (d). The degradation rate of 30% TiO_2/MIL-100(Fe) was the highest at 0.158 min^{-1}, which was 2.1 and 4.4 folds higher than that of MIL-100(Fe) (0.077 min^{-1}) and TiO_2 (0.036 min^{-1}), respectively (Fig. 6(b)–(d)). This result was observed because the rapid electron transfer between TiO_2 with co-exposed {001} and {101} facets and MIL-100(Fe) allowed the photogenerated

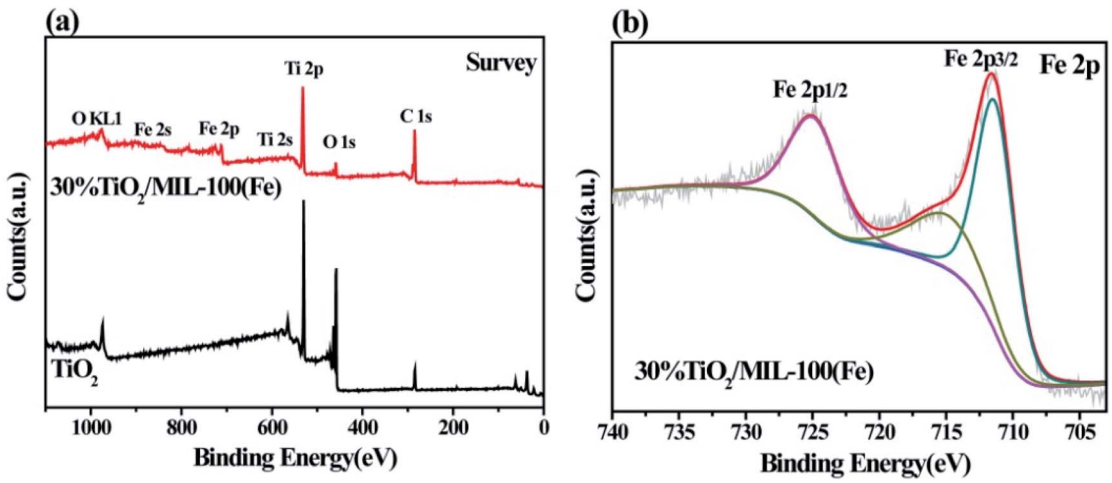

Fig. 4 XPS pattern measurements of neat TiO_2 and 30% TiO_2/MIL-100(Fe): (a) survey and (b) Fe 2p binding energy spectra.

Open Access Article. Published on 07 October 2019. Downloaded on 5/22/2026 4:35:28 AM.
This article is licensed under a Creative Commons Attribution-NonCommercial 3.0 Unported Licence.

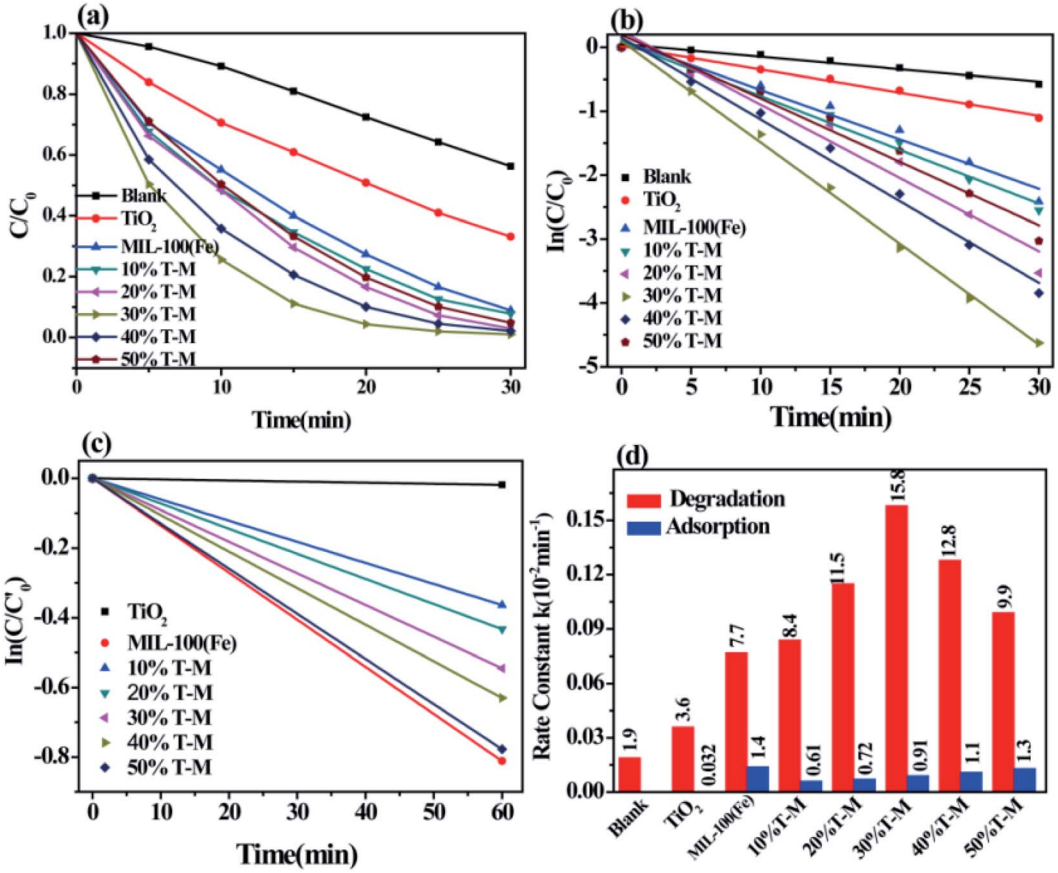

Fig. 6 (a) Control experiments for the photodegradation of MB with respect to different photocatalysts; (b) kinetics of MB degradation as a function of photocatalysts; (c) kinetics of MB adsorption as a function of photocatalysts; (d) catalytic rate constants of MB degradation and adsorption.C'_0 is the initial concentration of MB before dark adsorption, and C_0 is the concentration of MB before illumination. Reaction conditions: 5 mg photocatalyst, 100 mL of 10 mg L^{-1} MB aqueous solution.

electron–hole pairs to be efficiently separated. The MB adsorption kinetics equation (Fig. 6(c)–(d)) showed that the adsorption rates of MIL-100(Fe) and TiO_2/MIL-100(Fe) composites did not significantly improve, which is consistent with the BET results. Pure MIL-100(Fe) had the highest adsorption kinetics rate of 1.4×10^{-2} min^{-1}. The adsorption capacity of pure TiO_2 was low, and the adsorption amount of MB was approximately 1.9%. Combining TiO_2 and MIL-100(Fe) increased the adsorption kinetics rate of the TiO_2/MIL-100(Fe) complex because the high specific surface area and large pore size facilitated the capture of organic molecules and provided reaction sites. The interface channel also improved the adsorption capacity of the composite. At the same time, the synergy between the co-exposed {001} and {101} crystal facets of TiO_2 could also effectively promote photocarrier separation and further improve the photocatalytic efficiency.

The photodegradation cycle of the 30% {001} and {101} facet co-exposed TiO_2/MIL-100(Fe) composite was tested four times with MB to evaluate the reusability of the material. In each photodegradation experiment, the suspension was treated in the dark for 1 h to establish an adsorption–desorption equilibrium. The absorbance of MB from 4 cycles of photodegradation showed that the 30% TiO_2/MIL-100(Fe) composite maintained good adsorption and catalytic properties and had good stability (Fig. 7). Only 5 mg of the photocatalyst was slightly damaged by centrifugation and washing, thereby resulting in a slight decrease in the photocatalytic performance and adsorption performance.

According to the above results, the possible photocatalytic degradation mechanism of MB by the {001} and {101} facet co-exposed TiO_2/MIL-100(Fe) complexes was proposed (Fig. 8). Due to the charge transfer occurring between an inorganic semiconductor and the MOF, photogenerated electron–hole pair recombination can be substantially suppressed. Under visible light, photoexcited electrons (e^-) are transferred from the valence band to the conduction band on TiO_2, thereby forming holes (h^+) on the valence band.[10] The photoexcited electrons (e^-) are then transferred from the conduction band of TiO_2 to the conduction band of MIL-100(Fe) by the interactions between the TiO_2 and MIL-100(Fe) interfaces. This phenomenon also effectively suppresses the recombination of the photogenerated electron–hole pairs, thereby further improving the photocatalytic efficiency of the material. The

 This journal is © The Royal Society of Chemistry 2019

Open Access Article. Published on 07 October 2019. Downloaded on 5/22/2026 4:35:28 AM.
This article is licensed under a Creative Commons Attribution-NonCommercial 3.0 Unported Licence.

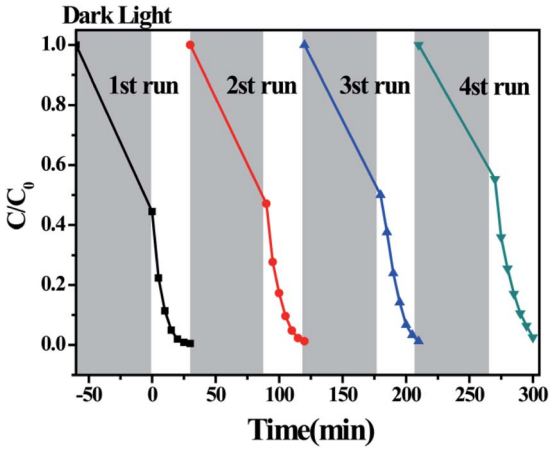

Fig. 7 Photocatalytic degradation of MB by 30% TiO_2/MIL-100(Fe) over four consecutive cycles.

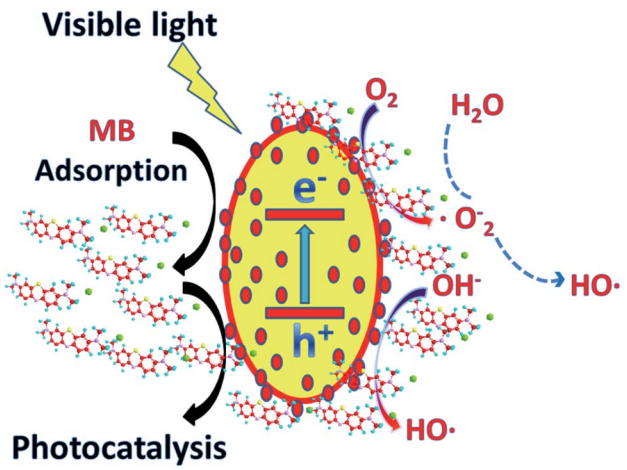

Fig. 8 Proposed mechanism for the photocatalytic degradation of MB by the {001} and {101} facet co-exposed TiO_2/MIL-100(Fe) composite.

photogenerated hole (e^-) in the valence band of TiO_2 oxidises MB or directly reacts with OH^- in H_2O to form a hydroxyl radical (·OH). The photogenerated electrons in the MIL-100(Fe) and TiO_2 conduction bands react with O molecules to form superoxide radicals ($\cdot O^{2-}$).[4,43] The MB molecules adsorbed on the surface of the composite are photodegraded by $\cdot O^{2-}$ and ·OH into CO_2, H_2O and other products. The TiO_2/MIL-100(Fe) composite with a larger pore size and specific surface area can effectively adsorb a certain amount of dye molecules and become the base of further photocatalytic reactions. The synergistic effect between the total exposure of the {001} and {101} TiO_2 crystal planes effectively improved the separation efficiency of the photogenerated electron–hole pairs. The special egg-like structure of the material had a larger pore size and specific surface area, which provided an effective channel for photoelectron electron–hole pair separation and a favourable place for the photocatalytic reaction. The interfacial effect of TiO_2 and MIL-100(Fe) also increased the photocatalytic efficiency.

4. Conclusion

In summary, the photocatalytic {001} and {101} facet co-exposed TiO_2/MIL-100(Fe) composite material was successfully prepared *via* a simple two-step hydrothermal method. A TiO_2/MIL-100(Fe) composite with 30% {001} and {101} facet co-exposed TiO_2 that maintained a complete egg-like morphology was prepared for the first time. The material had a higher specific surface area and pore diameter than pure MIL-100(Fe) under the same preparation conditions and exhibited excellent performance in the photocatalytic degradation of the organic dye MB. The efficiency of 30% TiO_2/MIL-100(Fe) in the photocatalytic degradation of MB in 30 min was as high as 99.02%. Photocatalytic experiments with 4 cycles showed that the reduction in the photocatalytic activity of the prepared composites was insignificant and it had good stability. The excellent performance in the photocatalysis was attributed to the synergistic effect between the {001} and {101} planes of TiO_2 and the interfacial effect between TiO_2 and MIL-100(Fe), and the egg-like morphology increased the specific surface area and pore size of the composite, which provided a channel for electron transfer to occur at the interface. To further improve solar energy utilisation, we will continue to conduct research on semiconductors and MOF composites.

Conflicts of interest

There are no conflicts to declare.

Acknowledgements

This work was supported by the National Natural Science Foundation of China (Grant no. 21671026) and Hunan Collaborative Innovation Center of Environmental and Energy Photocatalysis. The authors are also grateful to the aid provided by the Science and Technology Innovative Research Team in Higher Educational Institutions of Hunan Province.

Notes and references

1 Z. Zou, J. Ye, K. Sayama and H. Arakawa, *Nature*, 2001, **414**, 625.
2 C. B. D. Marien, T. Cottineau, D. Robert and P. Drogui, *Appl. Catal., B*, 2016, **194**, 1.
3 F. Cao, J. Xiong, F. Wu, Q. Liu, Z. Shi, Y. Yu, X. Wang and L. Liang, *ACS Appl. Mater. Interfaces*, 2016, **8**, 12239.
4 H.-Q. Xu, J. Hu, D. Wang, Z. Li, Q. Zhang, Y. Luo, S.-H. Yu and H.-L. Jiang, *J. Am. Chem. Soc.*, 2015, **137**, 13440.
5 X. Zeng, L. Huang, C. Wang, J. Wang, J. Li and X. Luo, *ACS Appl. Mater. Interfaces*, 2016, **8**, 20274.
6 P. Tan, A. Zhu, L. Qiao, W. Zeng, H. Cui and J. Pan, *J. Colloid Interface Sci.*, 2019, **533**, 452–462.
7 F. Yao, T. Jiao, J. Yin, L. Zhang, L. Zhang, J. Zhou and Q. Peng, *Nanoscale Res. Lett.*, 2019, **14**, 78.
8 Y. He, R. Wang, T. Jiao, X. Yan, M. Wang, L. Zhang, Z. Bai and Q. Zhang, *ACS Sustainable Chem. Eng.*, 2019, **7**, 10888–10899.

Open Access Article. Published on 07 October 2019. Downloaded on 5/22/2026 4:35:28 AM.
This article is licensed under a Creative Commons Attribution-NonCommercial 3.0 Unported Licence.

9 P. Tan, A. Zhu, Y. Liu, Y. Ma, W. Liu, H. Cui and J. Pan, *Inorg. Chem. Front.*, 2018, **5**, 679–686.
10 H. Xiang, H. Fang, D. J. Gosztola, J. Zhang, P. Jena and W.-N. Wang, *ACS Appl. Mater. Interfaces*, 2019, **11**, 12516.
11 G. Xiang, T. Li, J. Zhuang and X. Wang, *Chem. Commun.*, 2010, **46**, 6801.
12 A. Mercedes, E. Carbonell, B. Ferrer, F. X. Llabrési Xamena and H. Garcia, *Chem.–Eur. J.*, 2007, **13**, 5106.
13 W. Zeng, B. Yuan, S. Cao, Y. Ma, Y. Liu, A. Zhu and P. Tan, *ACS Appl. Mater. Interfaces*, 2018, **10**, 21328–21334.
14 L. Liu, Y. Jiang, H. Zhao, J. Chen, J. Cheng, K. Yang and Y. Li, *ACS Catal.*, 2016, **6**, 1097.
15 J. Ma, H. Wu, Y. Liu and H. He, *J. Phys. Chem. C*, 2014, **118**, 7434.
16 J. Yu, J. Low, W. Xiao, P. Zhou and M. Jaroniec, *J. Am. Chem. Soc.*, 2014, **136**, 8839.
17 J. Liu, D. Olds, R. Peng, Y. Lei, S. F. Guo, S. Qian, J. Keum, B. S. Guiton, Z. Wu and K. Page, *Chem. Mater.*, 2017, **29**, 5591.
18 S. L. James, *Chem. Soc. Rev.*, 2003, **32**, 276.
19 R. J. Drout, L. Robison and O. K. Farha, *Coord. Chem. Rev.*, 2019, **381**, 151.
20 T. Islamoglu, D. Ray, L. Peng, M. B. Majewski, I. Akpinar, X. Zhang, C. J. Cramer, L. Gagliardi and O. K. Farha, *Inorg. Chem.*, 2018, **57**, 13246.
21 L. Shi, T. Wang, H. Zhang, K. Chang, X. Meng, H. Liu and J. Ye, *Adv. Sci.*, 2015, **2**, 1500006.
22 C. Wang, J. Yin, S. Han, T. Jiao, Z. Bai, J. Zhou, L. Zhang and Q. Peng, *Catalysts*, 2019, **9**, 559.
23 R. Liang, R. Chen, F. Jing, N. Qin and L. Wu, *Dalton Trans.*, 2015, **44**, 18227.
24 K. Guesh, A. D. C. Clarice, Á. Mayoral, M. Díaz-García, I. Díaz and M. Sanchez-Sanchez, *Cryst. Growth Des.*, 2017, **17**, 1806.
25 N. Stock and S. Biswas, *Chem. Rev.*, 2011, **112**, 933.
26 J. W. Shin, M. Kim, J. Cirera, S. Chen, G. J. Halder, T. A. Yersak, F. Paesani, S. M. Cohen and Y. S. Meng, *J. Mater. Chem. A*, 2015, **3**, 4738.
27 D. Wang and Z. Li, *Catal. Sci. Technol.*, 2015, **5**, 1623.
28 Z. Zhang, X. Li, B. Liu, Q. Zhao and G. Chen, *RSC Adv.*, 2016, **6**, 4289.
29 D. Sun, Y. Fu, W. Liu, L. Ye, D. Wang, L. Yang, X. Fu and Z. Li, *Chem.–Eur. J.*, 2013, **19**, 14279.
30 L. Shen, R. Liang, M. Luo, F. Jing and L. Wu, *Phys. Chem. Chem. Phys.*, 2015, **17**, 117.
31 S. J. Garibay and S. M. Cohen, *Chem. Commun.*, 2010, **46**, 7700.
32 D. Sun and Z. Li, *J. Phys. Chem. C*, 2016, **120**, 19744.
33 D. Sun, L. Ye and Z. Li, *Appl. Catal., B*, 2015, **164**, 428.
34 D. Sun, W. Liu, Y. Fu, Z. Fang, F. Sun, X. Fu, Y. Zhang and Z. Li, *Chem.–Eur. J.*, 2014, **20**, 4780.
35 S.-N. Kim, J. Kim, H.-Y. Kim, H.-Y. Cho and W.-S. Ahn, *Catal. Today*, 2013, **204**, 85.
36 C. H. Hendon, D. Tiana, M. Fontecave, C. Sanchez, L. D'arras, C. Sassoye, L. Rozes, C. Mellot-Draznieks and A. Walsh, *J. Am. Chem. Soc.*, 2013, **135**, 10942.
37 H. Sheng, D. Chen, N. Li, Q. Xu, H. Li, J. He and J. Lu, *Chem. Mater.*, 2017, **29**, 5612.
38 N. Chang, H. Zhang, M.-S. Shi, L. Jia, W. Shao and H.-T. Wang, *Mater. Lett.*, 2017, **200**, 55.
39 D. Tilgner, M. Friedrich, J. Hermannsdörfer and R. Kempe, *ChemCatChem*, 2015, **7**, 3916.
40 S. Wan, M. Ou, Z. Qin and X. Wang, *Chem. Eng. J.*, 2019, **358**, 1287.
41 H. Liu, J. Zhang and D. Ao, *Appl. Catal., B*, 2018, **221**, 433.
42 C.-F. Zhanga, L.-G. Qiu, K. Fei, Y.-J. Zhua, Y.-P. Yuana, G.-S. Xua and X. Jianga, *J. Mater. Chem. A*, 2013, **1**, 14329.
43 X. Liu, R. Dang, W. Dong, X. Huang, T. Jia, H. Gao and G. Wang, *Appl. Catal., B*, 2017, **209**, 506.
44 J. Pan, G. Liu, G. Q. Lu and H.-M. Cheng, *Angew. Chem., Int. Ed.*, 2011, **50**, 2133.
45 Z. Zheng, B. Huang, J. Lu, X. Qin, X. Zhang and Y. Dai, *Chem.–Eur. J.*, 2011, **17**, 15032.
46 H. G. Yang, G. Liu, S. Z. Qiao, C. H. Sun, Y. G. Jin, S. C. Smith, J. Zou, H. M. Cheng and G. Q. Lu, *J. Am. Chem. Soc.*, 2009, **131**, 4078.
47 Y. Fang, W. Jia, G. Zeng, F. Jia, S. Zhang, Z. Peng and H. Zhang, *Chem. Eng. J.*, 2018, **337**, 532.

This journal is © The Royal Society of Chemistry 2019